# Reynolds stress budgets in Couette and boundary layer flows

Komminaho, Jukka; Skote, Martin

2002

https://hdl.handle.net/10356/81865

https://doi.org/10.1023/A:1020404706293

# Reynolds stress budgets in Couette and boundary layer flows

Jukka Komminaho and Martin Skote
Dept. of Mechanics, KTH,
SE-100 44, Stockholm, Sweden.

**Abstract**

Reynolds stress budgets for both Couette and boundary layer flows are evaluated and presented. Data are taken from direct numerical simulations of rotating and non-rotating plane turbulent Couette flow and turbulent boundary layer with and without adverse pressure gradient. Comparison of the total shear stress for the two types of flows suggests that the Couette case may be regarded as the high Reynolds number limit for the boundary layer flow close to the wall. The limit values of turbulence statistics close to the wall for the boundary layer for increasing Reynolds number approach the corresponding Couette flow values. The direction of rotation is chosen so that it has a stabilizing effect, whereas the adverse pressure gradient is destabilizing. The pressure-strain rate tensor in the Couette flow case is presented for a split into slow, rapid and Stokes terms. Most of the influence from rotation is located to the region close to the wall, and both the slow and rapid parts are affected. The anisotropy for the boundary layer decreases for higher Reynolds number, reflecting the larger separation of scales, and becomes close to that for Couette flow. The adverse pressure gradient has a strong weakening effect on the anisotropy. All of the data presented here are available on the web [36].

## 1  Introduction

The development of cheap, powerful, computers has lead to wide use of CFD codes for the prediction of turbulent flows. These codes almost always use turbulence models to try to capture the characteristics of the turbulent flow, and the prediction is no better than the weakest link in the computational chain. Often the weakest link is the turbulence model. But to develop better turbulence models one must have data to compare them against. In the early days of turbulence modelling one had to rely on indirect methods to test the various closure models. Experimental difficulties in measuring pressure and velocity with sufficient resolution did not make direct comparisons possible.

With the development of high-speed supercomputers, and new algorithms, [28, 29, 19, 4], it became possible to simulate turbulent flows directly without resorting to large eddy simulations or turbulence models. Now it became possible to evaluate any desirable quantity and use them to test turbulence models. The channel flow simulation by Kim et al. [16] was the first fully resolved sim-

ulation of a pressure-driven channel flow, and the database from the simulation has been used extensively to evaluate various turbulence models, see Mansour et al. [23].

There are few experimental studies of Couette flow with reports of turbulence statistics. In their study of Couette flow at a Reynolds number of 1300, Bech et al. [8] report both second and higher order statistics from both experiments and simulations. The agreement between the experiments and the simulation is good for the statistics, but their simulations do not fully capture the very large scale structures of the experiments. This is e.g. seen from the two-point correlations which are lower in the simulation than in the experiment. In the study by Bech and Andersson [7] they used three different sizes of their computational domain and observed large structures in one box, but not in the other two. The reason behind this is unclear.

Bech [6] presented Reynolds stress budgets from the simulation of Bech et al. [8], and they look very similar to the ones presented here, despite the higher Reynolds number in their simulation.

Bech and Andersson [5] made simulations with both positive and negative rotation with the same magnitude as in the present study, ($Ro = \pm 0.01$). For the positive rotation they decomposed the flow into secondary and turbulent flow and analyzed them. Their main conclusion was that the turbulence was damped for negative rotation. This was also found in the investigation by Komminaho et al. [17].

In the present paper the budget data for the Reynolds stresses in the Couette flow case are evaluated from flow fields of the plane Couette flow simulation by Komminaho et al. [17].

Data are also presented from three different turbulent boundary layers. One is a zero pressure gradient (ZPG) boundary layer, and two are boundary layers subject to an adverse pressure gradient (APG). Data from the ZPG boundary layer have not previously been presented. The simulation with a moderate APG (APG1) has been analyzed in Skote et al. [33], while the strong APG case (APG2) has been presented in Skote and Henningson [35].

The ZPG turbulent boundary layer flow has been studied in a large number of investigations, see e.g. the assessment of data by Fernholz [10]. Turbulent statistics close to the wall were obtained through DNS by Spalart [37], and were confirmed later in the experiment of a low Reynolds number ZPG turbulent boundary layer by Ching et al. [9]. Various Reynolds stress budgets from DNS of both ZPG and APG boundary layers were presented by Na and Moin [26]. Near-wall limit values of an APG boundary layer were also investigated in the DNS of Spalart and Watmuff [38] and in the experiment of Nagano et al. [27].

The results from the simulations of [17], [33] and [35] are documented here for future use in turbulence model development, in particular for near-wall modelling. The present plane Couette flow data are well suited for this purpose since the condition of a constant total shear is, unlike the situation in the boundary layer, fulfilled for all Reynolds numbers. The boundary layer data can be used for the development of low Reynolds number turbulence models.

## 2 Data analysis

One can write (see e.g. [12]) the Navier–Stokes and continuity equations in a rotating reference frame as,

$$\frac{\partial u_i'}{\partial t} + \frac{\partial}{\partial x_j}(u_i'u_j') = -\frac{1}{\rho}\frac{\partial p'}{\partial x_i} + \nu\frac{\partial^2 u_i'}{\partial x_j \partial x_j} + 2\epsilon_{ijk}u_j'\Omega_k \qquad (1)$$

$$\frac{\partial u_i'}{\partial x_i} = 0. \qquad (2)$$

The effect of the system rotation can be seen as a volume force in the fluid, also known as the Coriolis force and the centrifugal force. The Coriolis force is the last term in the momentum equation (1), and the centrifugal force has been included in the pressure. In the following we will use $u$, $v$, $w$ for $u_1$, $u_2$, $u_3$, and $x$, $y$, $z$ for the downstream, wall normal and spanwise directions.

Divide the flow into a mean and a fluctuating part, $u_i' = U_i + u_i$, where the mean part is defined as an ensemble average over $N$ different times, and also an average over the homogeneous directions ($x$ and $z$ in the Couette flow and $z$ in the boundary layer)

$$\overline{u_i'} \equiv U_i(y,t) = \frac{1}{NL_xL_z}\sum_{i=1}^{N}\int_0^{L_x}\int_0^{L_z} u_i'(x,y,z,t)\mathrm{d}x\mathrm{d}z. \qquad (3)$$

The Reynolds-average Navier–Stokes equation is now obtained as

$$\frac{\partial U_i}{\partial t} + \frac{\partial}{\partial x_j}(U_iU_j) = -\frac{1}{\rho}\frac{\partial P}{\partial x_i} + \nu\frac{\partial^2 U_i}{\partial x_j \partial x_j} - \frac{\partial}{\partial x_j}R_{ij} + 2\epsilon_{ijk}U_j\Omega_k \qquad (4)$$

where $R_{ij} = \overline{u_iu_j}$ is the velocity correlation tensor, and will here be referred to as the 'Reynolds stress tensor'.

The first term in the equation above is zero for time-independent flows. The statistics from our simulations were carefully shown to be stationary. The resolution of the simulations were checked by repeating the simulation on a finer grid in some cases. For all simulations the size of the computational box were shown to be sufficient. The velocity spectra showed that the resolution was adequate. For further information about the simulations see [17, 33, 35].

### 2.1 Couette data

Plane Couette flow is the flow between two parallel planes, moving in opposite directions with velocity $\pm U_w$ in the $x$-direction, at a distance $2h$. The system rotation $\Omega_3$ applied in the present work is around the $z$ axis. The non-dimensional rotation number is defined as,

$$Ro \equiv \frac{2\Omega_3 h}{U_w}. \qquad (5)$$

The various statistical quantities have been evaluated and averaged from 12 different velocity fields, and the average was taken in both $x$ and $z$ direction. The time between the samples was $T = 40$, where $T$ is based on the wall velocity $U_w$ and half channel height $h$. They are statistically independent for all but the very largest scales, see [17] where the time scale for the integral length scale ($\Lambda_{uux}$ defined as $\int R_{uu}(\Delta x)\mathrm{d}x$, $R_{uu}$ being the two-point velocity correlation) was found to be more than 50.

| Case | $Re_{\delta_*}$ | $Re_\Theta$ | $u_\tau$ | $U_\infty$ | $\beta$ |
|------|------|------|------|------|------|
| ZPG | 920 | 606 | 0.048 | 1.0 | 0.0 |
| APG1 | 1064 | 655 | 0.036 | 0.76 | 0.65 |
| APG2 | 2573 | 1309 | 0.020 | 0.60 | 5.0 |

Table 1: Reynolds number, friction velocity, freestream velocity and pressure gradient at the streamwise position where the Reynolds stress budgets have been evaluated.

## 2.2 Boundary layer data

The statistics have been produced in the same manner as in the Couette case, except for the important difference that the flow is not homogeneous in the streamwise ($x$) direction. The boundary layer is growing and developing in the $x-$direction due to the increasing Reynolds number. Thus, the statistics are unique for each streamwise position. However, here we are only dealing with the near-wall statistics, which in the viscous scaling should be independent of the Reynolds number. But in the low Reynolds number flows simulated with DNS, there is a small influence of the increasing Reynolds number. This effect is confined to the part very close to the wall ($y^+ < 3$). In the ZPG simulation e.g., the boundary layer undergoes a doubling of the Reynolds number, but the budgets fall on top of each other for different streamwise positions, except for the small increase of the values at the wall. The statistics are therefore shown for one streamwise position in all three cases.

The simulations APG1 and APG2 were performed with a pressure distribution leading to a self-similar boundary layer at high Reynolds numbers. The pressure gradient parameter $\beta$,

$$\beta \equiv \frac{\delta_*}{\tau_w} \frac{\mathrm{d}P}{\mathrm{d}x}, \tag{6}$$

defines the APG in these two simulations.

The Reynolds number at the position where the budgets have been evaluated is shown in table 1, together with the local value of the friction velocity, freestream velocity and pressure gradient parameter.

Another effect of the Reynolds number is the increasing length of the region with constant shear stress ($\tau^+$). This is illustrated in figure 1, which shows the total shear stress at two Reynolds numbers for the ZPG case, as well as for Couette flow. From figure 1 it is clear that the total shear stress for the boundary layer becomes more constant when the Reynolds number is increased. Since $\tau^+$ is constant for the Couette flow, it might be argued that this flow approximates a high Reynolds number boundary layer close to the wall.

## 2.3 Reynolds stress budget

The transport equations for the Reynolds stress tensor are obtained by multiplying (1) (after subtracting the mean equation (4)) with $u_j$, adding the corresponding equation with switched indices $i$, $j$ and ensemble averaging. The resulting equations read

$$\frac{\mathrm{D}R_{ij}}{\mathrm{D}t} \equiv \left( \frac{\partial}{\partial t} + U_j \frac{\partial}{\partial x_j} \right) R_{ij} = \mathcal{P}_{ij} - \varepsilon_{ij} + D_{ij} + \Pi_{ij} + G_{ij} + T_{ij} + C_{ij} \tag{7}$$
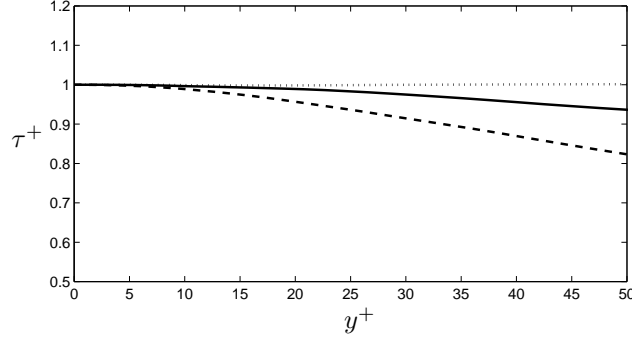
Figure 1: Total shear stress. Couette $(\cdots)$. Boundary layer: (- -) $Re_{\delta_*} = 539$, (—) $Re_{\delta_*} = 920$.

where

$$
\mathcal{P}_{ij} \equiv -\overline{u_i u_k}\frac{\partial U_j}{\partial x_k} - \overline{u_j u_k}\frac{\partial U_i}{\partial x_k}, \tag{8}
$$

$$
\varepsilon_{ij} \equiv 2\nu\overline{u_{i,k}u_{j,k}}, \tag{9}
$$

$$
D_{ij} \equiv \frac{\partial}{\partial x_k}\left(\nu R_{ij,k}\right), \tag{10}
$$

$$
\Pi_{ij} \equiv \frac{1}{\rho}\left(\overline{p\frac{\partial u_i}{\partial x_j}} + \overline{p\frac{\partial u_j}{\partial x_i}}\right), \tag{11}
$$

$$
G_{ij} \equiv -\frac{\partial}{\partial x_k}\left(\frac{1}{\rho}\overline{u_j p}\delta_{ik} + \frac{1}{\rho}\overline{u_i p}\delta_{jk}\right), \tag{12}
$$

$$
T_{ij} \equiv -\frac{\partial}{\partial x_k}\overline{u_i u_j u_k}, \tag{13}
$$

$$
C_{ij} \equiv -2\Omega_k\left(R_{lj}\epsilon_{ikl} + R_{il}\epsilon_{jkl}\right). \tag{14}
$$

Here $\mathcal{P}_{ij}$ is the production due to mean field gradients, whose trace $(\mathcal{P}_{ii})$ represents twice the production of turbulent energy, the transfer of energy from the mean flow to the turbulent fluctuations.

$\varepsilon_{ij}$ is the dissipation rate tensor, and $D_{ij}$ is the diffusion tensor. They both represent viscous effects, but whereas $D_{ij}$ is a molecular diffusion term acting to even out the turbulent stresses by spatial redistribution, $\varepsilon_{ij}$ act as a destruction term of turbulent energy (and stresses).

$\Pi_{ij}$ is the pressure-strain rate correlation tensor, which is traceless and represents inter-component transfer between Reynolds stress terms. $G_{ij}$ is the divergence of the pressure-velocity correlation, and represents transport driven by pressure fluctuations. This split in the above two terms is not unique, there are several different ways in which one may separate the pressure-velocity term when deriving the RST equations, but as the investigation by Groth [13] shows the above separation seems to make most physical sense.

$T_{ij}$ is the divergence of the triple correlation tensor, acting as a spatial redistribution term.

$C_{ij}$ is the traceless Coriolis tensor, which acts as a redistributive term among the stress components.
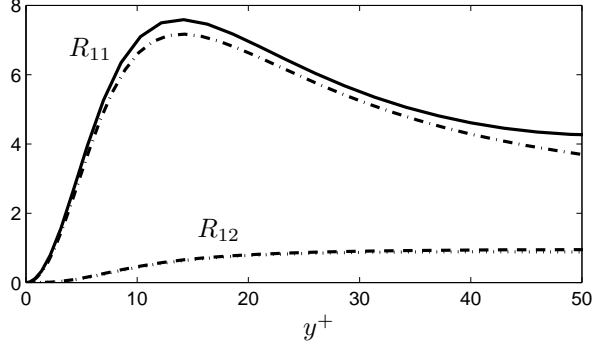
Figure 2: Reynolds longitudal and shear stress. Couette: (—) and (−−). Boundary layer: (− · −) and (· · ·).

The transport equation for the kinetic energy, $K \equiv \frac{1}{2}\mathcal{R}_{ii}$ is

$$\frac{\mathrm{D}K}{\mathrm{D}t} = \mathcal{P} - \varepsilon + \mathcal{D}, \tag{15}$$

where $\mathcal{P} = \frac{1}{2}\mathcal{P}_{ii}$ is the turbulent energy production, $\varepsilon = \frac{1}{2}\varepsilon_{ii}$ is the viscous dissipation, and $\mathcal{D} = \frac{1}{2}\left(T_{ii} + G_{ii} + D_{ii}\right)$ is the sum of the molecular and turbulent diffusion of $K$. This term acts as a spatial redistribution of $K$.

In a fully developed plane Couette flow, the flow is homogeneous in the $x$ and $z$ directions, and the relevant non-zero stresses are $R_{11}$, $R_{12}$, $R_{22}$ and $R_{33}$. The simulation flow fields represent a plane Couette flow at a Reynolds number $Re_\tau = u_\tau h/\nu = 52$ ($Re_\tau = 48$ for the rotating case) based on friction velocity $u_\tau$ and channel half-height $h$. This corresponds to a Reynolds number 750 based on wall-velocity and $h$. Despite this very low Reynolds number it is twice that of the transition Reynolds number of 360, see [22, 39, 18]. For the rotating case the rotation is as low as $Ro = -0.01$.

The budgets for the Reynolds stresses in the ZPG case are essentially the same as in the simulation by Spalart [37]. The moderate APG case, APG1, show very similar profiles in the Reynolds stress budgets as the APG simulation of Na and Moin [26]. The effects of the APG is stronger in the APG2 case, which has a skin friction approximately 60% of that in APG1. In this work, in contrast to the budgets in [37] and [26], the pressure term is divided into pressure-strain rate and pressure-velocity diffusion, for comparison with the Couette data.

The Reynolds stresses $R_{11}$ and $R_{12}$ are shown in figure 2 for the non-rotating Couette flow and the ZPG boundary layer flow. The maximum of $R_{11}$ is larger in the Couette flow, otherwise the profiles are similar. In figure 3, the streamwise velocity profiles for the same two flows are shown in a semilogarithmic plot. Here one can see that the Couette flow has a very small logarithmic region, while the boundary layer has developed such a region. Both flows obey the linear profile in the viscous sub-layer.

In figures 4 and 5 the budgets for the longitudal Reynolds stress are shown. The figures include both non-rotating and rotating Couette flow as well as all three boundary layer cases and the profiles from the ZPG case can be compared with the Couette case with zero rotation.

In figures 6 to 8 the budgets for the rest of the Reynolds stresses are shown for
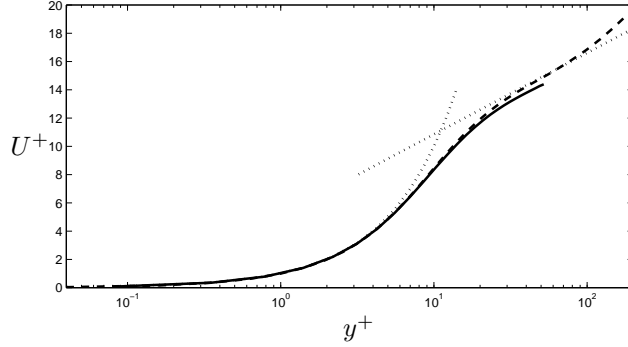
6

Figure 3: Mean streamwise velocity profiles. Couette: (—). Boundary layer: (- -). The dotted lines are the profiles $U^+ = y^+$ and $U^+ = 2.5 \ln y^+ + 5.1$.

the non-rotating Couette flow and ZPG boundary layer flow. The rotating and APG flows are just briefly discussed for these Reynolds stresses, and pictures of the budgets can be viewed on the web, see [36].

The terms in the budgets are shown as functions of the wall-normal distance $y^+ = yu_\tau/\nu$, where $u_\tau = \sqrt{\tau_w/\rho}$ is the friction velocity. Note that in the non-rotating case the Coriolis term, $C_{ij}$, is zero. All quantities are shown in $^+$-units, non-dimensionalized with $u_\tau^4/\nu$.

### 2.3.1 Longitudal Reynolds stress

One may note that the maximum of the production term $\mathcal{P}_{11}$ is 0.5. This is easily obtained by integrating the stream-wise momentum equation once, and multiplying with $\frac{dU^+}{dy^+}$. The advection term is zero in the Couette flow case and negligible in the near-wall region for boundary layers. By neglecting the advection term and assuming wall similarity, we obtain the following relation for the turbulence production:

$$\mathcal{P}_{11} \equiv -2\frac{\overline{uv}}{u_\tau^2}\frac{\mathrm{d}U^+}{\mathrm{d}y^+} = 2\frac{\mathrm{d}U^+}{\mathrm{d}y^+}\left(1 - \frac{\mathrm{d}U^+}{\mathrm{d}y^+} + \frac{\nu}{\rho u_\tau^3}\frac{\mathrm{d}P}{\mathrm{d}x}y^+\right), \qquad (16)$$

where the pressure gradient term is non-zero only in the adverse pressure gradient (APG) cases. The last term within the parenthesis can be rewritten as $\beta y^+/\delta_*^+$. From the above relation it follows that the maximum of $\mathcal{P}_{11}$ is 0.5 occurring at a position where $\mathrm{d}U^+/\mathrm{d}y^+ = 0.5$ for Couette flow and ZPG boundary layer. This holds irrespective of the value of the Reynolds number and the system rotation and was shown to accurately describe also the low-Reynolds number plane Couette flow simulation of Komminaho et al. [18] where the Reynolds number was as low as 375.

The overall character of the different terms in the Reynolds stress budget for $R_{ij}$ is the same as for the channel flow in [23]. Figure 4 shows that the production term $\mathcal{P}_{11}$ is the dominant positive term in the range $y^+ > 5$, and has a maximum of 0.5 in the buffer region, at $y^+ = 11$, falling to 0.10 in the centre of the channel. The location of the peak production can be found to be $y^+ \approx 11$ also in channel and pipe flow, see [31]. The non-zero production in the central region is a consequence of the non-zero mean shear in this region.
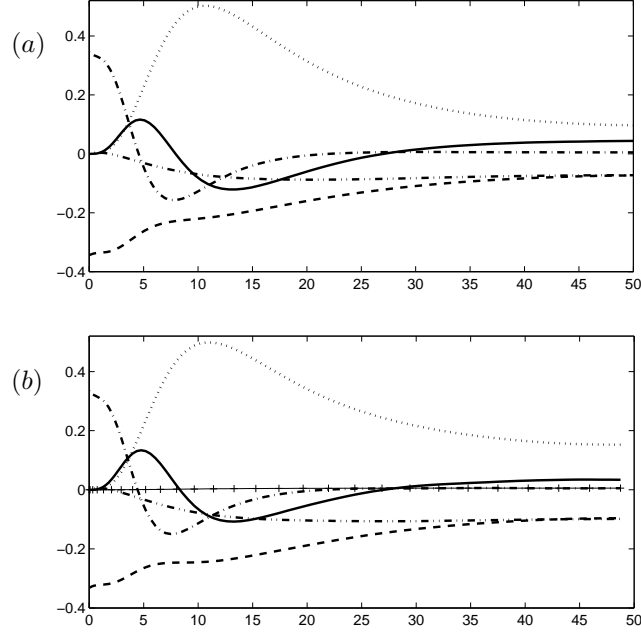
7

Figure 4: Terms in the Couette flow $R_{11}$-budget for ($a$) the non-rotating case and ($b$) the rotating case, $Ro = -0.01$. The different terms are: ($\cdots$) $\mathcal{P}_{11}$, (- -) $-\varepsilon_{11}$, (- · ·) $D_{11}$, (- · · · -) $\Pi_{11}$, (——) $T_{11}$, (+) $C_{11}$.

$\Pi_{11}$ is negative throughout the channel, thereby transferring energy from $R_{11}$ to $R_{22}$ and $R_{33}$. We will in section 2.3.2 see that $R_{22}$ receives energy only in a region away from the wall.

Despite the very low rotation rate for the Couette flow case the effects on some terms in the budgets are significant, away from the wall. The production $\mathcal{P}_{11}$ is about 60% larger in the centre of the channel for the rotating case. The dissipation $\varepsilon_{11}$ and the pressure-strain rate $\Pi_{11}$ are both 30% larger for the rotating case, whereas the redistributive term $T_{11}$ is about 20% smaller. Near the walls the non-rotating and rotating cases are very similar, as can be expected since the maximum production is 0.5 in both cases.

In figure 5a the budget for the longitudal Reynolds stress is shown for the ZPG case. The maximum of the production term $\mathcal{P}_{11}$ is 0.5 as in the Couette case. The other terms in the budget for $R_{11}$ corresponds very closely to those in the Couette case. The adverse pressure gradient increases the production $\mathcal{P}_{11}$ as seen in figures 5b and c. For APG1 it is 0.6 and APG2 0.9. The increase of the maximum is not explained by the contribution from the streamwise velocity gradient since that part of the production term is negligible close to the wall.

The increased value of $\mathcal{P}_{11}$ is thus explained from the contribution from the pressure gradient in equation (16). For the case APG2 we have a $\delta_*^+$ of 86 so that the last term within the parenthesis in equation (16) $\beta y^+/\delta_*^+$ is about 0.58 at $y^+ = 10$, i.e. near the maximum in production. It can, hence, be seen to be of the order one influence. Since $\beta y^+/\delta_*^+ = \beta y^+ \frac{U_\infty}{u_\tau}/Re_{\delta_*}$ we can see that the effect of the pressure gradient term decreases with increasing Reynolds number.

The position of the maximum of the production is shifted towards the wall,
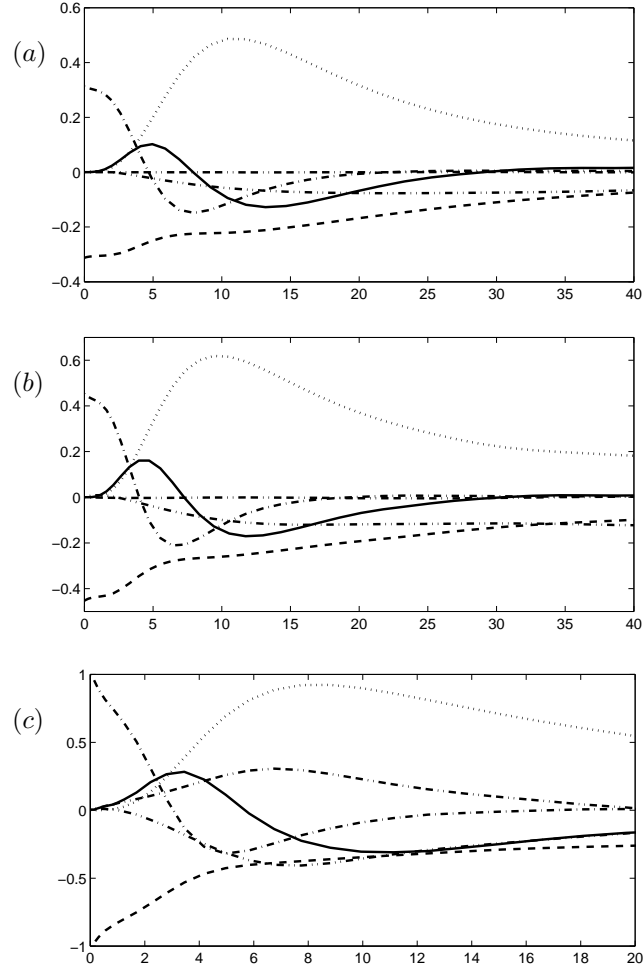
8

Figure 5: Terms in the $R_{11}$-budget for boundary layer flow ($a$) ZPG. ($b$) APG1. ($c$) APG2. The different terms are: ($\cdots$) $\mathcal{P}_{11}$, (- -) $-\varepsilon_{11}$, (- $\cdot$ -) $D_{11}$, (- $\cdot\cdot$ -) $\Pi_{11}$, (- - $\cdot\cdot$) $G_{11}$, (—) $T_{11}$.

most notably in the APG2 case (figure 5c).

Also the rest of terms show more extreme values in the APG cases, even though the shape of the profiles remain roughly the same. The enhanced values in the near-wall region are partly due to the decrease in the friction velocity (which all the terms in the budget are scaled with). The lower value of $u_\tau$ is a consequence of the adverse pressure gradient. One might argue that $u_\tau$ is not the correct scaling in an APG flow, since the total shear stress is not constant in this scaling. Alternative scalings, including a velocity scale dependent on the wall normal distance that produce a constant shear stress, are discussed by Skote and Henningson [34, 35].

Note that the term $G_{11}$, which is identically zero in the Couette case due to the homogeneous streamwise ($x$) direction, is zero also in the ZPG boundary layer. In the APG1 case the pressure gradient is not strong enough to affect this transport term. However, in the APG2 case a clear difference can be seen. Here $G_{11}$ contributes to the budget significantly. Another observation is that the collective contribution from $G_{11}$ and $\Pi_{11}$ to the budget remains constant since $\Pi_{11}$ decreases the same amount as $G_{11}$ increases. The two terms are parts of the original term including the pressure fluctuations in the budget, but have two different physical interpretations, which makes it difficult to draw conclusions from this observation. However, the split of the original pressure fluctuations term is important since the effects of the pressure gradient otherwise may not be observed.

### 2.3.2   Normal Reynolds stress

In figure 6a the budget for $R_{22}$ in the Couette flow case is shown. $\Pi_{22}$ is negative close to the wall, and positive towards the centre. Thus it transfers energy from the wall-normal component to the spanwise component ($\Pi_{33}$ is positive everywhere) near the wall, and receives energy from the longitudal component ($\Pi_{11}$ is negative everywhere) away from the wall. This reversal of the sign in $\Pi_{22}$ was attributed to the splatting effect in the LES study of turbulent channel flow by Moin and Kim [24] (see also the work by Hunt and Graham [15]). In the turbulence modelling context this effect is normally referred to as the wall-reflection contribution to the pressure strain. The attempts to model this (see [11]) typically assumes a variation on a length-scale of the order of the macro-scale. The present results and those of Aronson et al. [3] and Perot and Moin [30] however show that the effect is confined to a thin region near the wall. In some recent model development (see e.g.[32]) this effect is only indirectly accounted for through realizable models.

In figure 6b the budget for $R_{22}$ in the ZPG case is shown. All the terms show slightly lower values than in the Couette case, while the shapes of the profiles are similar.

For a figure of the rotating and APG flows, the reader is referred to [36]. There is only a small effect on the budget from the $C_{22}$ term in the rotating Couette flow, while all terms are increased in the APG boundary layer flow, particularly the pressure-strain rate ($\Pi_{22}$). The production term $P_{22}$ is identically zero in the Couette flow due to the homogeneous streamwise direction. It is essentially zero also in the non-homogeneous boundary layer flow, even in the strong APG flow case, see figure of $R_{22}$ budget for APG2 in [36].
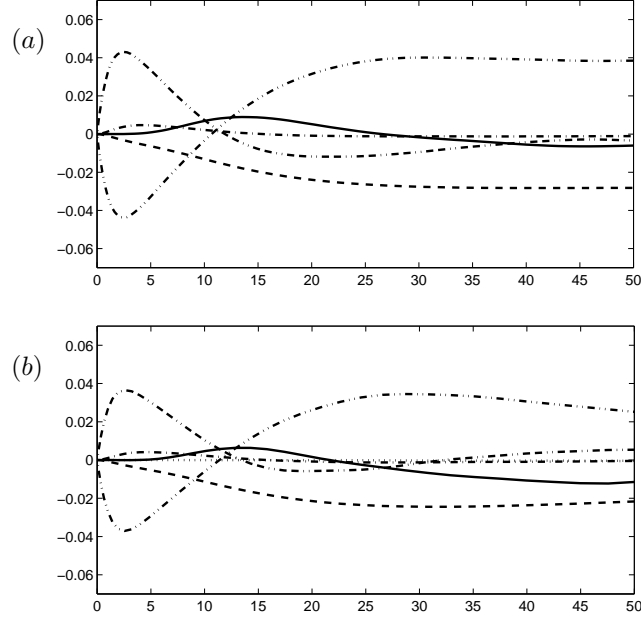
Figure 6: Terms in the $R_{22}$-budget for ($a$) the non-rotating Couette flow and ($b$) the ZPG boundary layer flow. The different terms are: $(\cdots)$ $\mathcal{P}_{22}$, $(\text{- -})$ $-\varepsilon_{22}$, $(\text{- $\cdot$ -})$ $D_{22}$, $(\text{- $\cdots$ -})$ $\Pi_{22}$, $(\text{- - - $\cdot$})$ $G_{22}$, $(\text{——})$ $T_{22}$.

### 2.3.3 Spanwise Reynolds stress

In the ZPG budget for the spanwise Reynolds stress, shown in figure 7b, the values of the different terms are, as in the $R_{22}$ budget, lower than in the Couette flow shown in figure 7a. The shapes of the profiles are similar to those in the Couette case.

No effect of the rotation could be seen close to the wall. The pressure gradient enhances the values (see [36]), but nothing else seems to be affected in the APG1 case. In APG2 however, the turbulent transport is of the same magnitude as the pressure-strain rate.

### 2.3.4 Reynolds shear stress

The budget for the Reynolds shear stress in Couette flow is presented in figure 8a. The pressure-strain rate ($\Pi_{12}$) and pressure diffusion ($G_{12}$) balance each other at the wall. This was also the case in channel flow simulation of Mansour et al. [23]. The value of $\Pi_{12}$ at the wall in Couette flow is more than twice the value found in [23].

The budget for the Reynolds shear stress in boundary layer flow is presented in figure 8b. The profiles are approximately the same as in the Couette case, except for the pressure-strain rate and pressure diffusion at the wall which shows larger values in the Couette case. The outer ($y^+ > 5$) values are however the same in the two flows.

The effect of rotation is to reduce the values of $\Pi_{12}$ and $G_{12}$ at the wall, and the budget resembles more the ZPG flow budget, see [36]. The term $C_{12}$ is
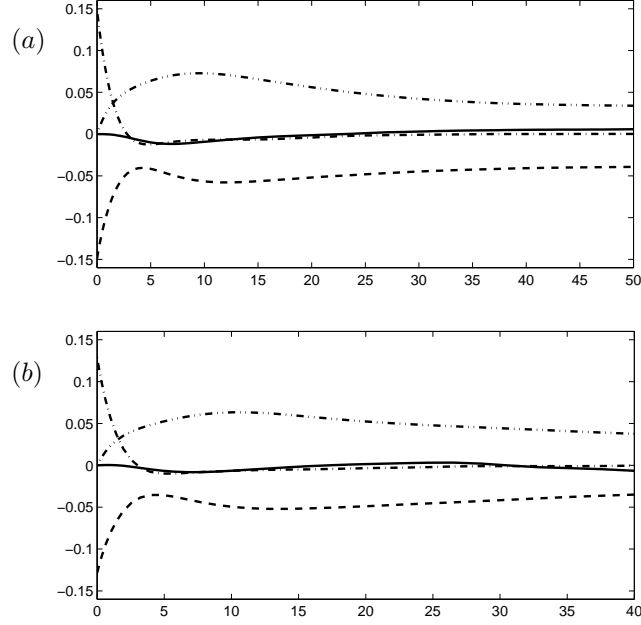
11

Figure 7: Terms in the $R_{33}$-budget for ($a$) the non-rotating Couette flow and ($b$) the ZPG boundary layer flow. The different terms are: (- -) $-\varepsilon_{33}$, (- · -) $D_{33}$, (- · · -) $\Pi_{33}$, (—) $T_{33}$.

small and has a limited effect on the budget.

The values at the wall in the boundary layer flow are increased by the APG. In the stronger APG2 case, also the region away from the wall is affected, [36].

## 2.4   Near-wall behavior

There is a balance between dissipation and viscous diffusion on the wall. From the data in figures 4–7 we may also compute the dissipation rate anisotropies, $e_{ij} = \varepsilon_{ij}/\varepsilon - \frac{2}{3}\delta_{ij}$. The limiting values of these (along with the stress anisotropies $a_{ij} = R_{ij}/K - \frac{2}{3}\delta_{ij}$) are given in table 2 and compared with the predictions obtained by the algebraic dissipation rate anisotropy models of Hallbäck et al. [14] and Sjögren and Johansson [32].

Table 2: Couette data: Limiting values for the stress anisotropies $a_{ij}$ and dissipation rate anisotropies $e_{ij}$, and comparison with models.

| component | 1,1 | 2,2 | 3,3 |
|---|---|---|---|
| $a_{ij}$ | 0.72 | $-\frac{2}{3}$ | $-0.05$ |
| $e_{ij}$ | 0.73 | $-\frac{2}{3}$ | $-0.06$ |
| $(e_{ij})_{\text{Hallbäck}}$ | 0.67 | $-\frac{2}{3}$ | $0.00$ |
| $(e_{ij})_{\text{Sjögren}}$ | 0.72 | $-\frac{2}{3}$ | $-0.05$ |

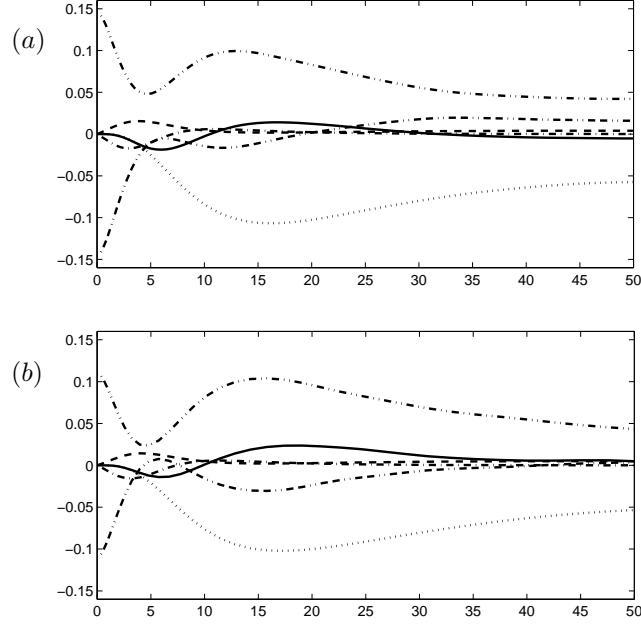The agreement is quite satisfactory for both models in the Couette case,

Figure 8: Terms in the $R_{12}$-budget for ($a$) the non-rotating Couette flow and ($b$) the ZPG boundary layer flow. The different terms are: ($\cdots$) $\mathcal{P}_{12}$, (- -) $-\varepsilon_{12}$, (- $\cdot$ -) $D_{12}$, (- $\cdot\cdot\cdot$ -) $\Pi_{12}$, (- - - $\cdot$) $G_{12}$, (—) $T_{12}$.

| component | 1,1 | 2,2 | 3,3 |
|---|---|---|---|
| $a_{ij}$ | 0.76 | $-\frac{2}{3}$ | $-0.09$ |
| $e_{ij}$ | 0.76 | $-\frac{2}{3}$ | $-0.09$ |
| $(e_{ij})_{\text{Hallbäck}}$ | 0.50 | $-\frac{2}{3}$ | 0.17 |
| $(e_{ij})_{\text{Sjögren}}$ | 0.76 | $-\frac{2}{3}$ | $-0.09$ |

Table 3: Boundary layer data: Limiting values for the stress anisotropies $a_{ij}$ and dissipation rate anisotropies $e_{ij}$, and comparison with models.

while the Sjögren and Johansson model is in better agreement with DNS data for the ZPG boundary layer. In the Hallbäck et al. model $e_{ij}$ is given by

$$e_{ij} = \left[1 + \alpha(\frac{1}{2}\text{II}_a - \frac{2}{3})\right] a_{ij} - \alpha(a_{ik}a_{kj} - \frac{1}{3}\text{II}_a\delta_{ij}), \quad \alpha = \frac{3}{4}, \qquad (17)$$

whereas in the Sjögren and Johansson model we have

$$e_{ij} = (1 - \frac{1}{2}F)a_{ij}, \quad F = 1 - \frac{9}{8}(\text{II}_a - \text{III}_a). \qquad (18)$$

In the above expressions we have introduced the two nonzero invariants of the anisotropy tensor,

$$\text{II}_a = a_{ij}a_{ji}, \qquad (19)$$
$$\text{III}_a = a_{ij}a_{jk}a_{ki}. \qquad (20)$$

13

| Case $Re_{\delta_*}$ | $u^+_{rms}/y^+$ | $v^+_{rms}/{y^+}^2$ | $w^+_{rms}/y^+$ | $-\overline{uv}^+/{y^+}^3$ | $\varepsilon^+$ |
|---|---|---|---|---|---|
| ZPG 539 | 0.385 | 0.0112 | 0.232 | 0.00099 | 0.203 |
| ZPG 920 | 0.398 | 0.0119 | 0.252 | 0.00102 | 0.223 |
| Couette | 0.414 | 0.0135 | 0.268 | 0.00121 | 0.246 |
| Channel [25] | 0.397 | 0.0113 | 0.250 | 0.00095 | 0.221 |
| Channel [1] | 0.409 | 0.012 | 0.261 | 0.0011 | 0.227 |

Table 4: Limit values for $y^+ \to 0$.

| Case | $u^+_{rms}/y^+$ | $v^+_{rms}/{y^+}^2$ | $w^+_{rms}/y^+$ | $-\overline{uv}^+/{y^+}^3$ | $\varepsilon^+$ |
|---|---|---|---|---|---|
| APG1 $\beta = 0.65$ | 0.476 | 0.0177 | 0.344 | 0.00181 | 0.346 |
| APG2 $\beta = 5.0$ | 0.728 | 0.0470 | 0.764 | 0.00598 | 1.35 |
| Couette $Ro = -0.01$ | 0.387 | 0.0124 | 0.243 | 0.00093 | 0.238 |

Table 5: Limit values for $y^+ \to 0$.

The latter model gives $e_{ij} = a_{ij}$ as limiting value in the two-component limit, such as on a solid wall. This describes the situation very accurately in both flow cases. Note that the Sjögren and Johansson model is a higher order model than the Hallbäck et al. model, and both satisfy the rapid distortion theory (RDT) limit of $e_{ij} = a_{ij}/2$, whereas only the former model satisfy the near-wall limit of $e_{ij} = a_{ij}$.

For this extremely low Reynolds number the dissipation rate is highly anisotropic also at the centreline in the Couette case.

Some important limiting values at the wall are given in table 4 and 5. The dependence of the Reynolds number in the boundary layer is strong as seen in table 4. All the values increase for higher Reynolds number, but they do not reach the values of the Couette flow. Hence, one might argue that the Couette data constitute a high Reynolds number limit for the boundary layer. The channel flow data is taken from a recent DNS at $Re_\tau = 590$ by Moser et al. [25], and at $Re_\tau = 640$ by Abe et al. [1]. All the limiting values for these quite high Reynolds number channel flows are lower than the ones from the Couette data, and close to the values for the boundary layer at $Re_{\delta_*} = 920$.

We have here shown that the boundary layer limiting values approach the Couette data when the Reynolds number increases. However, the limiting values in the Couette data may be Reynolds number dependent and increase with Reynolds number. Higher Reynolds number Couette flow simulations are needed to clarify this issue.

The effect of the APG on the boundary layer is quite severe as seen from table 5. All limit values are increased when the boundary layer is subject to an APG. The rotation in the Couette case has the opposite effect; all limit values decreases.

## 2.5 Anisotropy tensor

The Reynolds stress anisotropy tensor $a_{ij}$ has, as already mentioned above, two nonzero invariants, $\mathrm{II}_a$ and $\mathrm{III}_a$. All anisotropic states can be represented in
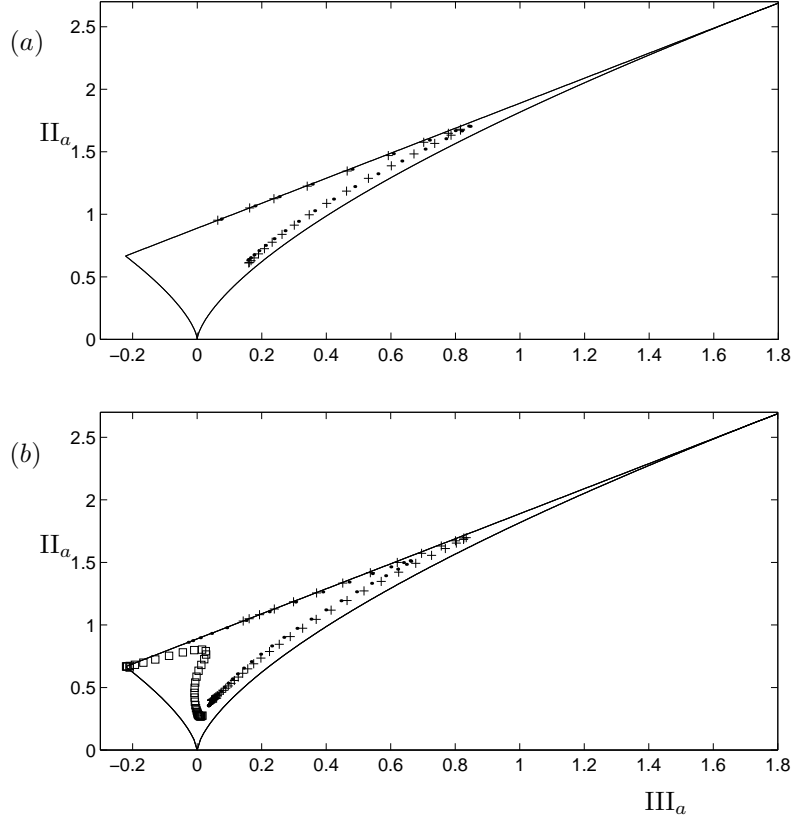
14

Figure 9: The anisotropy invariant map. a) AIM paths for the non-rotating ($+$) and rotating ($\cdot$) case. b) AIM paths for ZPG ($+$) ; APG1 ($\cdot$); APG2 ($\square$).

the anisotropy invariant map (see [21]) which are bounded by the lines $8/9 + \mathrm{III}_a = \mathrm{II}_a$ and $6\mathrm{III}_a^2 = \mathrm{II}_a^3$. They represent two-component and axisymmetric turbulence, respectively.

In figure 9a the AIM paths for both the non-rotating and rotating Couette cases are shown. Their main characteristics are the same as for the channel flow simulations of Moser et al. [25] and the Couette flow simulation with $Ro = -0.01$ of Bech and Andersson [5]. Close to the wall the turbulence is very near the two-component limit, approaching the one-component limit near the edge of the viscous sub-layer. At $y^+ \approx 8$ the AIM path turns towards the isotropic state. For the present cases the $Re_\tau$ is so low that there is nearly no real log-layer in the profiles with corresponding agglomeration of points in the AIM, as observed in the higher-$Re$ channel flow simulations. One may note that this absence of a developed log-layer is also clear from the mean velocity profile in figure 3.

The AIM paths for the boundary layer flows are shown in figure 9b. The ZPG case is very similar to the Couette flow. There is some agglomeration of points at the end of the path which is $y^+ \approx 150$ (for ZPG). The path for APG1 starts at a lower value of $\mathrm{III}_a$ and represents a lower degree of anisotropy than in the ZPG case. The end of the APG1-path is at $y^+ \approx 100$. The differences

15

| Case $Re_{\delta_*}$ | max $\mathrm{II}_a$ |
|---|---|
| ZPG 539 | 1.77 |
| ZPG 920 | 1.70 |
| APG1 | 1.51 |
| APG2 | 0.80 |
| Couette | 1.71 |
| Channel [25] | 1.72 |
| Channel [1] | 1.69 |

Table 6: Maximum values for $\mathrm{II}_a$.

between ZPG and APG1 are not so large in comparison with the APG2 case, where the path starts in the lower left corner and represents much lower degrees of anisotropy than in the other cases. This is explained by the less structured turbulence in a strong APG boundary layer. The path for APG3 was terminated at $y^+ \approx 50$, and is similar to the anisotropy states from a backward-facing step, see the investigation by Sjögren and Johansson [32] of the data from a backward-facing step simulation by Le and Moin [20].

The maximum anisotropy occurs at $y^+ \sim 8$ ($\mathrm{II}_a$ and $\mathrm{III}_a$ reach maxima at this point). The maximum decreases with increasing Reynolds number, see table 6 for values of $\mathrm{II}_a$. This reflects the increasing scale separation for higher Reynolds numbers, which leads to a more isotropic state. The same effect was reported by in the investigation of turbulent boundary layer and channel flow by Antonia et al. [2].

A similar scenario can be seen when the APG is increasing, the pressure gradient seems to have a large effect on the magnitude of the anisotropy. The location of the maximum of $\mathrm{II}_a$ moves slightly towards the wall with increasing APG.

The maximum $\mathrm{II}_a$ for the Couette flow is close to the ZPG boundary value at the higher Reynolds number. The value is the same for the rotating and non-rotating cases.

For comparison we also show the maximum $\mathrm{II}_a$ for the highest Reynolds number ($Re_\tau = 590$) channel flow of Moser et al. [25] and ($Re_\tau = 640$) by Abe et al. [1]. The value for the latter case is a little lower, but still close to the Couette flow value.

## 2.6 Pressure-strain rate split

The results from a split of the pressure-strain rate is here presented for the Couette flow. The result from taking the divergence of the Navier–Stokes equation is a Poisson equation for the pressure,

$$\frac{\partial^2 p}{\partial x_i \partial x_i} = -\frac{\partial}{\partial x_i}\frac{\partial}{\partial x_j}(u_i' u_j') - 2\epsilon_{ijk}\Omega_j \frac{\partial u_k'}{\partial x_i} \tag{21}$$

with the wall boundary condition,

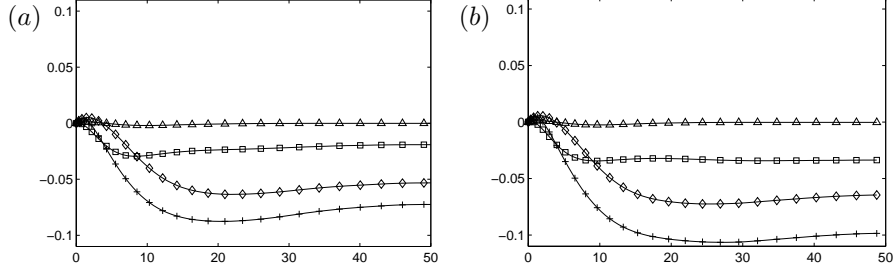$$\frac{\partial p}{\partial y} = \frac{1}{Re}\frac{\partial^2 v'}{\partial y^2} - 2U\Omega_3. \tag{22}$$

Figure 10: The $\Pi_{11}$-split for $(a)$ the non-rotating case and $(b)$ the rotating case, $Ro = -0.01$. The different terms are: $(+)$ $\Pi_{11}^{(\text{tot})}$, $(\diamond)$ $\Pi_{11}^{(\text{s})}$, $(\square)$ $\Pi_{11}^{(\text{r})}$, $(\triangle)$ $\Pi_{11}^{(\text{St})}$.
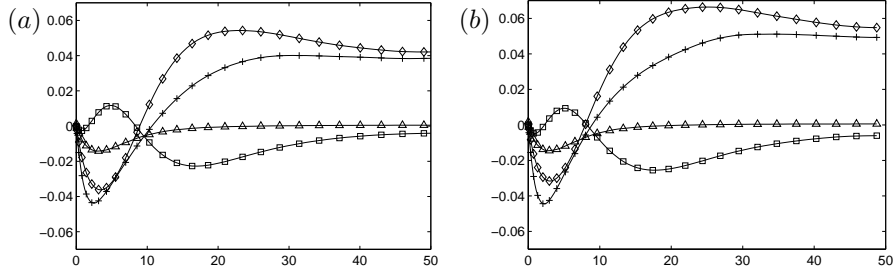


Figure 11: The $\Pi_{22}$-split for $(a)$ the non-rotating case and $(b)$ the rotating case, $Ro = -0.01$. The different terms are: $(+)$ $\Pi_{22}^{(\text{tot})}$, $(\diamond)$ $\Pi_{22}^{(\text{s})}$, $(\square)$ $\Pi_{22}^{(\text{r})}$, $(\triangle)$ $\Pi_{22}^{(\text{St})}$.

By splitting the source term in the Poisson equation into one part containing the mean velocity gradient and one part containing only gradients of the fluctuating part, we may derive equations for the rapid, slow and Stokes pressure, respectively.

$$\nabla^2 p^{(\text{r})} = -2\left(\frac{\partial U_i}{\partial x_k} + \epsilon_{ijk}\Omega_j\right)\frac{\partial u_k}{\partial x_i}, \qquad \frac{\partial p^{(\text{r})}}{\partial y} = 0 \tag{23}$$

$$\nabla^2 p^{(\text{s})} = -\frac{\partial u_i}{\partial x_j}\frac{\partial u_j}{\partial x_i}, \qquad \frac{\partial p^{(\text{s})}}{\partial y} = 0 \tag{24}$$

$$\nabla^2 p^{(\text{St})} = 0, \qquad \frac{\partial p^{(\text{St})}}{\partial y} = \frac{1}{Re}\frac{\partial^2 v}{\partial y^2} - 2U\Omega_3. \tag{25}$$

The Stokes pressure is solely due to the inhomogeneous boundary condition, and may be added to either the rapid or the slow pressure. Note that the last term in the boundary condition for the Stokes pressure is non-zero only for a moving wall, e.g. Couette flow. Restricting ourself to the present case of a channel with two homogeneous directions the rapid part simplifies further,

$$\nabla^2 p^{(r)} = -2\frac{\text{d}U}{\text{d}y}\frac{\partial v}{\partial x} - 2\Omega_3\omega_3. \tag{26}$$

The split into rapid, slow and Stokes pressure-strain rate can be seen in figure 10–13 for $\Pi_{11}$–$\Pi_{12}$. The slow part of $\Pi_{11}$ is larger than the rapid except
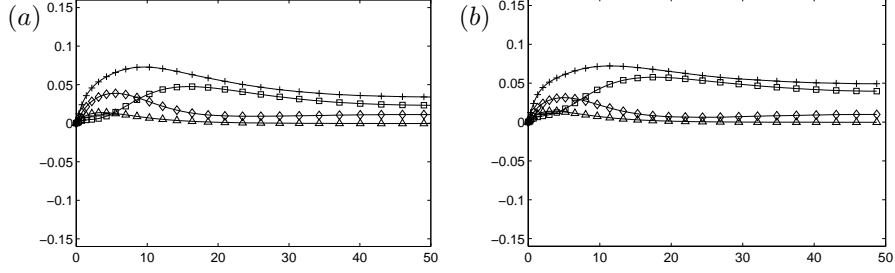
Figure 12: The $\Pi_{33}$-split for $(a)$ the non-rotating case and $(b)$ the rotating case, $Ro = -0.01$. The different terms are: $(+)$ $\Pi_{33}^{(\text{tot})}$, $(\diamond)$ $\Pi_{33}^{(\text{s})}$, $(\square)$ $\Pi_{33}^{(\text{r})}$, $(\triangle)$ $\Pi_{33}^{(\text{St})}$.
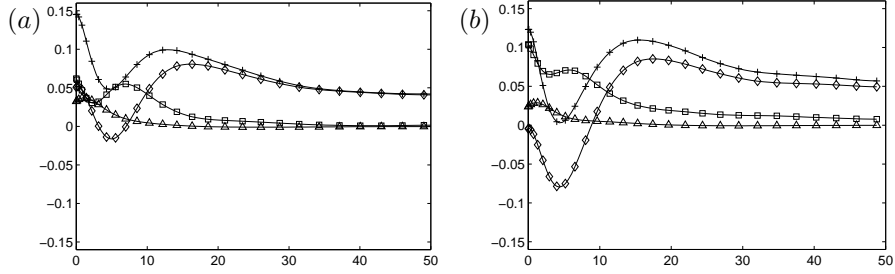


Figure 13: The $\Pi_{12}$-split for $(a)$ the non-rotating case and $(b)$ the rotating case, $Ro = -0.01$. The different terms are: $(+)$ $\Pi_{12}^{(\text{tot})}$, $(\diamond)$ $\Pi_{12}^{(\text{s})}$, $(\square)$ $\Pi_{12}^{(\text{r})}$, $(\triangle)$ $\Pi_{12}^{(\text{St})}$.

near the wall, $y^+ < 10$, where the mean velocity gradient is large. The rapid part is more affected by the rotation than the slow part.

Also for the $\Pi_{22}$-term the slow part is larger than the rapid part, and contribute most to the pressure-strain rate. Here the slow part is more affected by the rotation.

For the $\Pi_{33}$-term the rapid part contributes most, except for $y^+ < 10$, and is also most affected by the rotation.

Both the slow and rapid parts are significantly affected by the rotation for the $\Pi_{12}$-term in the region close to the wall. The total effect on the $\Pi_{12}$-term is not as great as on the individual terms, but results in lower values of $\Pi_{12}$ close to the wall.

The Stokes part for $\Pi_{22}$, $\Pi_{33}$ and $\Pi_{12}$ is significant only in the region $y^+ < 10$, and for $\Pi_{11}$ it is negligible throughout the channel.

The general character and amplitude of the various pressure-strain rate terms are almost identical even for $Re = 375$, despite the low Reynolds number.

# 3   Summary

We have used the Couette flow simulation data of Komminaho et al. [17] and the boundary layer data of Skote et al. [33] and Skote and Henningson [35] to compute terms in the transport equation for the Reynolds stresses. For the Couette flow we have also presented data for a split of the pressure-strain rate

term in rapid, slow and Stokes. Data were presented for both rotating (slow stabilizing rotation) and non-rotating Couette flow. One can see a small effect of the rotation on the limiting values at the wall in the Couette flow, but it is small as could be expected, since it is a very slow rotation. In the centre of the channel the budgets were strongly influenced by the rotation.

Boundary layer data were presented for one zero pressure gradient flow and two adverse pressure gradient flows. Strong influence on the budgets from the adverse pressure gradient were detected.

The Couette data we have presented here fulfill some important characteristics of high Reynolds number flow close to the wall. These are constant shear stress and a maximum production of turbulent kinetic energy of 1/4. However, other important properties of turbulence, such as scale separation, are not fulfilled.

The near-wall limits of turbulence statistics were shown to increase with Reynolds number in the zero pressure gradient boundary layer, but they did not reach the values obtained from the Couette flow. The hypothesis that the Couette flow is the high Reynolds number limit close to the wall cannot be verified with the present data. Also, the limiting values in the Couette data may be Reynolds number dependent and increase with Reynolds number. Higher Reynolds number Couette flow simulations are needed to clarify this issue. With the super-computers available in the near future, simulations of higher Reynolds number flows in simple geometries will be a feasible task. It would be interesting to compare the limit values presented here with a simulation for higher Reynolds number.

Two algebraic models of the dissipation rate anisotropies were investigated. For the Couette and ZPG boundary layer flows, the higher order model showed better agreement with DNS data. More challenging cases for models are the rotating Couette and APG boundary layer flows. With the data presented here, one can compare turbulence models which include rotation or APG.

The maximum anisotropy was shown to decrease with increasing Reynolds number for the ZPG flow. The APG has a strong dampening effect on the anisotropy, both regarding the maximum value and in the anisotropy invariant map. The maximum anisotropy in the Couette flow has approximately the same value as in the ZPG flow at the highest Reynolds number.

The pressure-strain rate split in the Couette case showed that both the slow and rapid parts are affected by the rotation, while the Stokes part remained unaffected. The strongest influence of the rotation could be detected for the non-diagonal term ($\Pi_{12}$).

## Acknowledgements

## References

[1] Abe, H., H. Kawamura, and Y. Matsuo: 2001, 'Direct numerical simulation of a fully developed turbulent channel flow with respect to the Reynolds

number dependence'. *J. Fluids Engng* **123**, 382–393.

[2] Antonia, R. A., L. Djenidi, and P. R. Spalart: 1994, 'Anisotropy of the dissipation tensor in a turbulent boundary layer'. *Phys. Fluids* **6**(7), 2475–2479.

[3] Aronson, D., A. V. Johansson, and L. Löfdahl: 1997, 'Shear-free turbulence near a wall'. *J. Fluid Mech.* **338**, 363–385.

[4] Basdevant, C.: 1983, 'Technical improvement for direct numerical simulation of homogeneous three-dimensional turbulence'. *J. Comp. Phys.* **50**(2), 209–214.

[5] Bech, K. and H. I. Andersson: 1996, 'Secondary flow in weakly rotating turbulent plane Couette flow'. *J. Fluid Mech.* **317**, 195–214.

[6] Bech, K. H.: 1995, 'Simulation of rotating and non-rotating turbulent plane Couette flow'. Ph.D. thesis, Department of Applied Mechanics, Thermodynamics and Fluid dynamics, Norwegian Institute of Technology, Trondheim.

[7] Bech, K. H. and H. I. Andersson: 1994, 'Very-large-scale structures in DNS'. In: P. R. Voke, L. Kleiser, and J.-P. Chollet (eds.): *Direct and Large-Eddy Simulations I*. Dordrecht: Kluwer, pp. 13–24.

[8] Bech, K. H., N. Tillmark, P. H. Alfredsson, and H. I. Andersson: 1995, 'An investigation of turbulent Couette flow at low Reynolds numbers'. *J. Fluid Mech.* **286**, 291–325.

[9] Ching, C. Y., L. Djenidi, and R. A. Antonia: 1995, 'Low-Reynolds-number effects in a turbulent boundary layer'. *Exps. Fluids* **19**, 61–68.

[10] Fernholz, H. H. and P. J. Finley: 1996, 'The incompressible zero-pressure-gradient turbulent boundary layer: An assessment of the data'. *Prog. Aerospace Sci.* **32**, 245–311.

[11] Gibson, M. M. and B. E. Launder: 1978, 'Ground effects on pressure fluctuations in the atmospheric boundary layer'. *J. Fluid Mech.* **86**, 491–511.

[12] Greenspan, H. P.: 1990, *The theory of rotating fluids*. Breukelen Press.

[13] Groth, J.: 1991, 'Description of the pressure effects in the Reynolds stress transport eqautions'. *Phys. Fluids A* **3**(9), 2276–2277.

[14] Hallbäck, M., J. Groth, and A. V. Johansson: 1990, 'An algebraic model for nonisotropic turbulent dissipation rate term in Reynolds stress closures'. *Phys. Fluids A* **2**(10), 1859–1866.

[15] Hunt, J. C. R. and J. M. R. Graham: 1978, 'Free-stream turbulence near plane boundaries'. *J. Fluid Mech.* **84**, 209–235.

[16] Kim, J., P. Moin, and R. Moser: 1987, 'Turbulence statistics in fully developed channel flow'. *J. Fluid Mech.* **177**, 133–166.

[17] Komminaho, J., A. Lundbladh, and A. V. Johansson: 1996, 'Very large structures in plane turbulent Couette flow'. *J. Fluid Mech.* **320**, 259–285.

[18] Komminaho, J., A. Lundbladh, and A. V. Johansson: 1997, 'Determination of the transition Reynolds number in plane Couette flow through study of relaminarization'. In: C. Liu and Z. Liu (eds.): *First AFOSR Int. Conf. on DNS/LES*. Ruston, LA, USA, pp. 233–240.

[19] Kreiss, H.-O. and J. Oliger: 1972, 'Comparison of accurate methods for the integration of hyperbolic equations'. *Tellus* **24**, 199–215.

[20] Le, H. and P. Moin: 1992, 'Direct numerical simulation of turbulent flow over a back-ward facing step'. In: *Annual Research Briefs*. Stanford Univ. Center for Turbulence Research, pp. 161–173.

[21] Lumley, J. L. and G. R. Newman: 1977, 'The return to isotropy of homogenous turbulence'. *J. Fluid Mech.* **82**, 161–178.

[22] Lundbladh, A. and A. V. Johansson: 1991, 'Direct simulation of turbulent spots in plane Couette flow'. *J. Fluid Mech.* **229**, 499–516.

[23] Mansour, N. N., J. Kim, and P. Moin: 1988, 'Reynolds-stress and dissipation-rate budgets in a turbulent channel flow'. *J. Fluid Mech.* **194**, 15–44.

[24] Moin, P. and J. Kim: 1982, 'Numerical investigation of turbulent channel flow'. *J. Fluid Mech.* **118**, 341–377.

[25] Moser, R. D., J. Kim, and N. N. Mansour: 1999, 'Direct numerical simulation of turbulent channel flow up to $Re_\tau = 590$'. *Phys. Fluids* **11**(4), 943–945.

[26] Na, Y. and P. Moin: 1996, 'Direct Numerical Simulation of Studies of Turbulent Boundary Layers with Adverse Pressure Gradient and Separation'. Technical Report TF-68, Thermosciences Division, Department of Mechanical Engineering, Stanford University.

[27] Nagano, Y., M. Tagawa, and T. Tsuji: 1992, 'Effects of Adverse Pressure Gradients on Mean Flows and Turbulence Statistics in a Boundary Layer'. In: F. Durst, R. Friedrich, B. E. Launder, F. W. Schmitd, U. Schumann, and J. H. Whitelaw (eds.): *Turbulent Shear Flows 8*. pp. 7–21.

[28] Orszag, S. A.: 1969, 'Numerical methods for the Simulation of Turbulence'. *Phys. Fluids Suppl. II* **12**, 250–257.

[29] Orszag, S. A.: 1970, 'Transform method for the calulation of Vector-coupled sums: Application to the spectral form of the vorticity equation'. *J. Athmosph. Sci.* **27**, 890–895.

[30] Perot, J. B. and P. Moin: 1995, 'Shear-free turbulent boundary layers. Part 1. Physical insights into near-wall turbulence'. *J. Fluid Mech.* **295**, 199–227.

[31] Sahay, A. and K. Sreenivasan: 1999, 'The wall-normal position in pipe and channel flow at which viscous and turbulent shear stresses are equal'. *Phys. Fluids* **11**(10), 3186–3188.

[32] Sjögren, T. and A. V. Johansson: 2000, 'Development and calibration of algebraic nonlinear models for terms in the Reynolds stress transport equations'. *Phys. Fluids* **12**(6), 1554–1572.

[33] Skote, M., R. A. W. M. Henkes, and D. S. Henningson: 1998, 'Direct Numerical Simulation of Self-Similar Turbulent Boundary Layers in Adverse Pressure Gradients'. *Flow, Turbulence and Combustion* **60**, 47–85.

[34] Skote, M. and D. Henningson: 1999, 'Analysis of the data base from a DNS of a separating turbulent boundary layer.'. Center for Turbulence Research, Annual Research Briefs 1999, 225–237.

[35] Skote, M. and D. S. Henningson: 2001, 'Direct numerical simulation of a separating turbulent boundary layer'. *J. Fluid Mech.* (Submitted).

[36] Skote, M. and J. Komminaho: 2001, 'http://www.fluidosol.se/html_lib/ data_jukka.html'.

[37] Spalart, P. R.: 1988, 'Direct simulation of a turbulent boundary layer up to $Re_\theta = 1410$'. *J. Fluid Mech.* **187**, 61–98.

[38] Spalart, P. R. and J. H. Watmuff: 1993, 'Experimental and numerical study of a turbulent boundary layer with pressure gradients'. *J. Fluid Mech.* **249**, 337–371.

[39] Tillmark, N. and P. H. Alfredsson: 1992, 'Experiments on transition in plane Couette flow'. *J. Fluid Mech.* **235**, 89–102.